ACS Catalysis
Research Article
pubs.acs.org/acscatalysis

Mechanistic Study of Pt–Re/γ-Al_2O_3 Catalyst Deactivation by Chemical Imaging of Carbonaceous Deposits Using Advanced X-ray Detection in Scanning Transmission Electron Microscopy

Sergio I. Sanchez,* Mark D. Moser, and Steven A. Bradley

UOP LLC–A Honeywell Company, 25 E. Algonquin Road, Des Plaines, Illinois 60017-5017, United States

Supporting Information

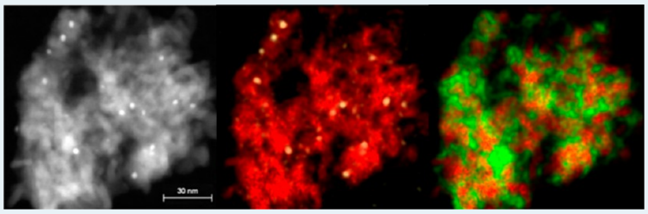

ABSTRACT: Accumulation of carbonaceous deposits (also known industrially as "coke") on catalytic active sites derived from process conditions has been a long-standing problem in industrial catalysis. Over accumulation of the deposits ultimately lead to deactivation; thus, characterization of coke evolution becomes critical toward developing catalytic materials with improved stability. This study focuses on extending an understanding of how and where coke forms on Pt–Re/γ-Al_2O_3, an industrial catalyst used in reforming processes. With the use of spherical aberration-corrected scanning transmission electron microscopy (C_s-STEM) and enhanced energy dispersive X-ray spectroscopy (EDX), we characterize the Pt–Re metal sites and show, to our knowledge, the first examples of chemically imaged subnanometer particles and also the first to use chemical maps to identify coke location on a catalyst. A two-step mechanism is reported based on the results whereby coke appears to stream from the metal function of the catalyst resulting in heterogeneous coverage.

KEYWORDS: *reforming, Pt–Re, deactivation, EDX, coking, STEM*

1. INTRODUCTION

To understand structure-performance relationships in heterogeneous catalysts it is necessary to conduct structural and chemical analyses at atomic length scales. Spherical aberration-corrected scanning transmission electron microscopy (C_s-STEM) has enabled analysis of atomic scale features in a variety of supported-metal catalytic systems, providing information on morphology, active sites, and dispersion of the metal function.[1−4] High-angle annular dark-field (HAADF) electron imaging can chemically discriminate between elements by scattering angle which scales with atomic number ($\sim Z^2$).[4] For more complicated systems such as bi- or trimetallic particles spectroscopic forms of analyses are required to assess stoichiometry. Electron energy loss spectroscopy (EELS) coupled with C_s-STEM is able to obtain atomic resolution microanalysis data of thin films[4] and also noble metal electrocatalysts.[5] It is sensitive, however, to sample thickness and more problematic for high atomic number elements ($Z_{Zn} > 30$)[6] of which metal nanoparticles on heterogeneous catalysts are often composed. Energy dispersive X-ray spectroscopy (EDX) offers accessibility to a wider range of X-ray lines facilitating the identification and quantification of a broader range of elements. Unfortunately, characterization of successively smaller features in materials chemistry has, until recently, challenged the detection limits of conventional EDX systems on electron microscopes (solid angle of 0.1 sr, collecting approximately 1% of the generated X-rays).[7] A historic weakness of EDX has been the poor detection of light elements (such as C, O, and N) but with the development of higher solid-angle silicon-drift detector (SDD) technology and high-brightness emission sources significant advances in EDX detection limits (solid angle of 0.7 sr) for both heavy ($\sim Z_{Zn} > 30$) and light elements (O, N, and C) have been achieved.[7] This is particularly critical for beam sensitive samples such as catalysts.[8]

Typical heterogeneous catalysts are composed of small metal particles supported on a semimetal oxide substrate. Since the metal particles in a freshly prepared industrial, heterogeneous catalyst are of subnanometer dimensions[9−11] the associated volumes generating characteristic X-rays are quite small (for an 8 Å cluster there are approximately 15–20 atoms).[12] The combination of so few atoms with a beam sensitive support emphasizes the necessity for improved signal collection efficiency. Advances in light element detection (especially C) become beneficial in the analysis of processed/spent catalysts where carbonaceous deposits/coke accrue on the catalyst with processing time-on-stream (TOS). The ability to analyze C signals on a spent catalyst enables studying catalyst deactivation as a function of the accrued coke. Here we demonstrate that it is now possible to chemically image subnanometer metal particles on a semimetal oxide support while simultaneously identifying the presence of coke. Collectively, the ensemble of data provides definitive insight toward understanding the relationship between coke formation and active sites on Pt–

Received: September 13, 2013
Revised: December 5, 2013
Published: December 9, 2013

Re/γ-Al_2O_3, an industrially important catalyst used in the reformation of hydrocarbon.[13]

Reforming catalysts are used to convert naphtha streams (a mixture composed of alkanes and cycloalkanes) into high-octane streams of isoalkanes and aromatics.[13−15] These bifunctional catalysts incorporate two active components: an acidic function and a metallic function. The γ-Al_2O_3 contains the acidic sites which generate carbenium ions leading to molecular rearrangements[13,14] (isomerization, cyclization, and dehydrocyclization) while the metallic component is responsible for hydrogenation and dehydrogenation reactions.[13,14] Reforming catalysts generally implement both Pt and Re as the metal function, though through the years supplementary components have been included. Previous investigations of reforming catalysts have focused on the valence state of the Re,[16−18] the relative importance of electronic and atomic structural effects as a function of metal particle geometry,[19−21] metal atom species mobility,[19,22,23] but perhaps most importantly, the mechanism of catalyst stabilization during the reforming process conditions through Re addition.[20,23,24] Additionally, there have been studies proposing the location and varieties of coke on the catalyst.[25,26] The scope of the current work is 3-fold: (1) to characterize the freshly prepared catalyst; (2) to characterize the catalyst after being pilot plant tested with the added task of monitoring coke development, and (3) to correlate the effects of catalyst testing while monitoring changes to the catalyst system and expand upon accepted views related to the mechanism of catalyst deactivation by way of coke formation.

2. EXPERIMENTAL METHODS

2.1. Pt−Re/γ-Al_2O_3 Catalyst Preparation. Pt−Re/γ-Al_2O_3 catalysts were prepared by impregnating 1.6 mm γ-Al_2O_3 extrudates (UOP LLC) with an acidic solution of chloroplatinic acid [$H_2PtCl_6\cdot(H_2O)_6$ (aq); FW = 409.81 g/mol], perrhenic acid [$Re_2O_7(OH_2)_2$ (aq); FW = 251.21 g/mol] in a 1.3:1 (Pt:Re) molar ratio. The solution was diluted to 90% of the volume of the support with water. The solution and support were added in a rotating, steam-jacketed glass evaporator where the mixture was rotated and heated until free-rolling was achieved. After impregnation the unreduced catalyst was loaded into a tube furnace and calcined at 510 °C for a period of 8 h. Reduction of the calcined product was carried out at 510 °C in a flow of 15% mol H_2 (g) (balance He (g)) for 2 h in a tube furnace. Prior to (and after) the introduction of H_2 (g) at 510 °C the furnace was purged with N_2 (g).

2.2. Catalyst Testing. Pilot plant testing involved reacting the catalyst for specified periods of time (10 and 96 h) to systematically check the coke levels. Pilot plant operations were conducted at a total pressure of 200 psig by cofeeding 1.5 mol of H_2 (g) with 1 mol of naphtha. Per process hour 150 cm^3 of naphtha were streamed over 60 cm^3 of catalyst. The hydrocarbon feed used in the pilot plant testing had an initial boiling point of 79 °C and an end boiling point of 166 °C. Catalyst testing was run until a target research octane number (RON) of 101.5 was achieved. Final products were analyzed by online gas chromatography (Hewlett-Packard) and knock engine analysis (CFR Research Engine).

2.3. Catalyst Characterization. *Compositional Analysis.* The freshly prepared catalyst was analyzed by inductively coupled plasma (ICP) analysis using a benchtop Optima 8300 ICP Optical emission spectrometer (ICP-OES, PerkinElmer Inc.) with a full-wavelength-range CCD array detector to determine the metal levels on the catalyst (0.35 wt % Pt, 0.25 wt % Re). For the spent catalysts coke/C levels were determined using a CS600-Series combustion analyzer (LECO Corporation) equipped with an infrared spectrometer for CO_2 detection (Measured C levels were 0.6 wt % C, for the sample 10 h TOS; and 11 wt % C, for the sample 96 h TOS).

Scanning Transmission Electron Microscopy. Samples were prepared by grinding the as-received extrudates into a powder with a mortar and pestle. Powders were deposited directly onto 200 mesh holey carbon Nylon grids (Pacific Grid Tech) for imaging (particle sizing and atomic resolution) and chemical analyses (excluding the chemical mapping). Loaded grids were then inserted into the Titan 80−300 electron microscope equipped with ChemiSTEM technology (FEI Company; Hillsboro, U.S.A.) and a CEOS GmbH (Heidelberg, Germany) CESCOR spherical-aberration probe-corrector. The ChemiSTEM system comprises a design that includes a high-brightness emission source (X-FEG Schottky) for enhanced beam current, and four integrated 30 mm^2 FEI-designed silicon drift detector(s) (SDD) into the objective lens for a total collection area and solid angle measurement of 120 mm^2 and 0.7 sr, respectively. Windowless SDD detectors boost the collection efficiency of light element (i.e., C, N, O, etc.) detection which otherwise would preclude the absorption of low energy X-rays (<1 keV) by a polymer film or obstruction by its support grid (collectively the "window").

Imaging was conducted in STEM mode with the microscope operating at 200 keV and an electron probe focused to ~0.8 Å, with a beam dosage of 800 e/Å$^2\cdot$s (based on the current collected on the fluorescent screen). The camera length was set to 160 mm to improve particle support contrast. For bimetallic Pt−Re particle sizing, C_s-STEM micrographs were captured at 1.3 MX magnification with a pixel calibration of 56.7 pm^2 resulting in a data set of 1024 × 1024 pixels. Images were processed and particle measurements made using Image-Pro software. Nanoparticle diameters were determined taking the average of every possible diameter that traverses the center of a particle between two tangent points. Atom counting was accomplished by collecting a series of images at atomic resolution (5.1 Mx magnification) over sufficiently thin regions of the support. Intensity contributions from the individual atoms were counted for scanned areas of 265 nm^2 for each of the three samples. Topography was ignored for simplicity and thus individual atom density per square area represented the number of individual atoms per area of image as opposed to surface area of the support.

Chemical analysis of individual nanoparticles was done by point analysis using a defocused electron probe to minimize beam damage. Spectra were collected at 640 kX magnification. Collection times were sustained below 20 s to avoid beam damage by overexposure. Both the L_α and L_β X-ray lines were used for Pt and Re during quantitative analysis.

Sample preparation for 2-dimensional chemical maps required the use of 200 μm Si grids coated with 15 nm thick Si film (SiMPore UltraSM) as the use of Nylon grids would result in spurious C signals related to the TEM grid and not coke on the sample. Multiple maps were examined with exposure times varying between 10−20 min using the K_α X-ray emission line for C for quantitative purposes. Regions of interest were compared before and after data collection to ensure substantial changes to the sample had not occurred as a result of the exposure to the incident radiation. A GIF Tridiem

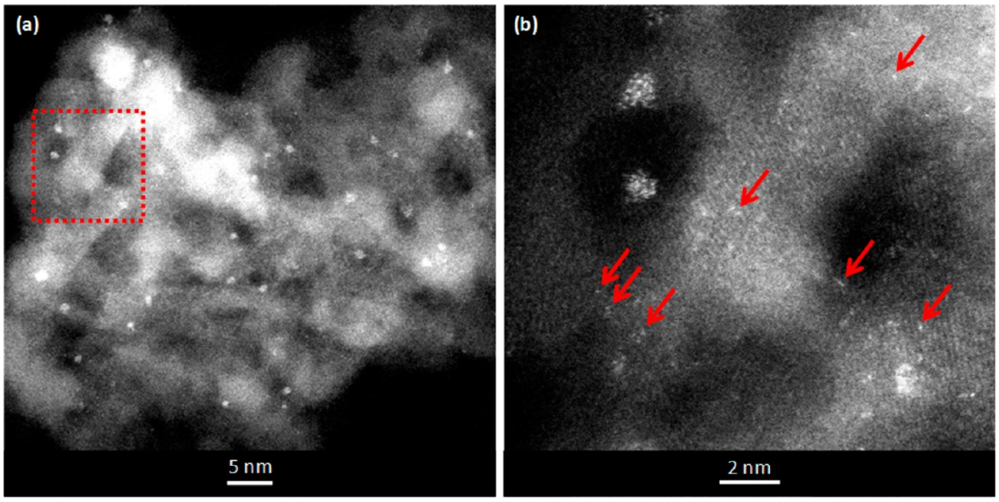

Figure 1. (**a**) C_s-STEM micrograph showing the metal dispersion of the Pt–Re/γ-Al_2O_3 catalyst, the boxed region is magnified in (**b**) to display disordered atomic structure of the Pt–Re nanoparticles and the presence of several dispersed atoms (arrows).

Table 1. Statistical Results from the Particle Sizing Analysis Conducted on the Catalysts

sample	mean particle size (nm)	standard deviation (±nm)	standard error (±nm)	median particle size (nm)	number examined
fresh Pt–Re/γ-Al_2O_3 (0 h TOS)	0.75	0.17	0.005	0.73	1134
fresh Pt–Re/γ-Al_2O_3 (10 h TOS)	0.77	0.18	0.005	0.77	1291
fresh Pt–Re/γ-Al_2O_3 (96 h TOS)	0.78	0.18	0.005	0.78	1259

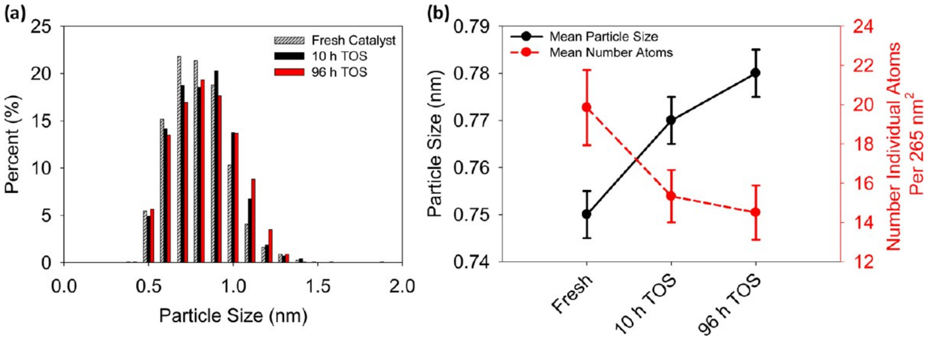

Figure 2. (**a**) Size distribution histograms combined for the fresh and spent (10 and 96 h TOS) catalysts. (**b**) Shows the change in average number of individual atoms per 265 nm^2 area as a function of TOS overlaid with the changes to mean particle size as a function of TOS. The error bars are the standard error values reported in Tables 1 and 2

postcolumn energy filter (Gatan, Inc.) was used for electron energy loss spectroscopy (EELS) analyses. EELS data were carried out with a 50 μm limiting aperture at 910 kX magnification using a 38 mm camera length. The energy range of the EELS spectrum acquired was from 110 to 520 eV covering a scanned region of 30 × 30 pixels calibrated at 1.74 nm^2 resulting in a total integration time of 13 s. Drift correction was enabled during spectrum imaging to compensate for changes to sample position during both EDX and EELS data acquisition.

3. RESULTS

Figure 1 shows a low-magnification C_s-STEM micrograph of the freshly prepared (untested) Pt–Re/γ-Al_2O_3 catalyst (Figure 1a) side-by-side with an atomic resolution micrograph from the same region (Figure 1b). Pt–Re metal nanoparticles are clearly well dispersed throughout the γ-Al_2O_3 support (Figure 1a). The boxed region in panel 1a is magnified in panel 1b to show that in addition to bimetallic particles a series of individual Pt and Re metal atoms unassociated with the nanoparticles are dispersed across the γ-Al_2O_3 lattice (arrows). The mean particle size for the untested sample was calculated to be 7.5 Å with a standard deviation (±) of 1.7 Å (standard error = 0.05 Å), denoting a narrow size distribution (Table 1). After pilot plant testing for 10 and 96 h there appears to be only a slight increase in particle size (7.7 ± 1.8 Å and 7.8 ± 1.8 Å, respectively; Figure 2a and Table 1). It is noteworthy to mention that particles falling below 4 Å (lattice constant for Pt = 3.92 Å) were not permitted in the particle sizing analysis thereby precluding contributions from individually dispersed atoms, dimers and/or trimers.

The number of individual atoms for a limited set of atomic resolution images was tallied to approximate the differences in the number of individual atoms per image for each sample. Mean values as a measure of atom density for a fixed area are reported for the three samples in Table 2. Figure 2b makes a comparison between mean particle size and the number of atoms in a series of atomic resolution images, each covering a scanned area of 265 nm^2 for all three samples. Inspection of the

Table 2. Statistical Results from the Quantitative Approximation of Atoms per 265 nm^2 Area

sample	mean no. individual atoms	standard deviation	standard error
fresh Pt−Re/γ-Al_2O_3 (0 h TOS)	19.8	6.6	1.9
fresh Pt−Re/γ-Al_2O_3 (10 h TOS)	15.3	4.6	1.3
fresh Pt−Re/γ-Al_2O_3 (96 h TOS)	14.5	4.8	1.4

data shows a decrease in the average number of individual atoms with TOS coincident with an increase in mean particle size, albeit the standard deviation is relatively high indicating significant overlap in the breadth of data between samples (Table 1 and 2). Sample images comparing the number of individual atoms for the fresh 0 h TOS and spent 96 h TOS samples are presented in Figure S1 (Supporting Information).

EDX spectra were collected for multiple individual nanoparticles for each of the samples to evaluate stoichiometric changes as a function of TOS. Results in Figure 3 indicate a broad range of stoichiometries for the Pt−Re metal particles with a large fraction of them composed of only Pt, for all three samples. Comparison of the three samples elicits two interesting features: (1) an overall shift in the distribution of the data toward Re-enrichment with increasing TOS; and (2) a decrease in the fraction of Pt-only particles with increasing TOS (Pt-only particles: Fresh 0 h TOS 46%, 10 h TOS 42%, and 96 h TOS 33%; Table 3). Despite the increased association between Pt and Re with TOS the particles on average are Pt-enriched: 85% Pt-15% Re (0 h TOS), 81% Pt-19% Re (10 h TOS), and 76% Pt-24% Re (96 h TOS); as outlined in Table 3.

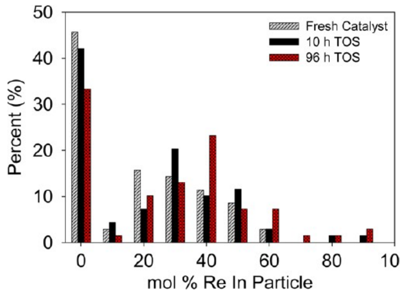

Figure 3. Distribution of particle stoichiometries for the Pt−Re/γ-Al_2O_3 catalyst at different stages. Data for the fresh catalyst (gray), 10 h TOS (black), and 96 h TOS (red) are shown.

Table 3. Statistical Results from the EDX Analysis of Pt−Re Particles[a]

sample	% Pt only particles	mean particle stoichiometry
fresh Pt−Re/γ-Al_2O_3 (0 h TOS)	46%	85% Pt 15% Re
fresh Pt−Re/γ-Al_2O_3 (10 h TOS)	42%	81%Pt 19% Re
fresh Pt−Re/γ-Al_2O_3 (96 h TOS)	33%	76% Pt 24% Re

[a] Data derived from distributions in Figure 3.

Figures 4 and 5 show chemical maps displaying the location of coke deposits (C K_α X-ray signals) after 10 and 96 h TOS, respectively. Figure 4a places the micrograph image from which the chemical maps were derived adjacent to a two-dimensional chemical map/spectral images for Al and C. Overlaying the C and Al EDX chemical maps (Figure 4b) show the C signal/coke (green) to be homogeneously deposited on the γ-Al_2O_3 support, depicted by the Al signal (red), just above background. Attempts were also made to collect chemical maps of the subnanometer Pt−Re nanoparticles in the 10 h spent sample. Arrows in the Pt, Al and Re, Al (Figure S2, Supporting Information) in the maps denote particle positions in reference to those found in Figure 4a. While a weak agreement exists the signals were barely above background despite an exposure time of 20 m.

Analogous data are presented in Figure 5 for the 96 h spent catalyst. In contrast to the more homogeneous distribution of the coke in the 10 h sample Figure 5b shows the C signal to be heterogeneous. Regions rich in coke are seen adjacent to regions relatively depleted of coke. Figure 5c and 5d show the spectral images for Pt, Al and Re, Al; respectively. The slightly larger particle size measured in Figure 1 generates a more pronounced signal in the chemical image allowing a correlation between the particles in the micrograph (Figure 5a) and the Pt signals in Figure 5c. For the Re, Al chemical image (panel 5d) the correlation is not apparent likely because of the difference in bulk metal loadings (0.35 wt % Pt versus 0.25 wt % Re) and the fact that on average the particles appear to be more Pt-enriched in both the fresh and the spent state (Figure 3 and Table 3). Figure 5e combines the maps of panels 5b and 5c (5d excluded for clarity) to assess the relationship between the coke and the bimetallic particles.

Electron energy loss spectroscopy (EELS) analyses were employed to determine whether the formed coke was formed of graphitic or amorphous carbon (Figure 6). Figure 6a and 6b show EELS spectra at spots annotated in the micrograph image (6c). An EELS chemical map was extracted from the spectral regions flanking the C signal (energy window 265−345 eV) to generate the chemical map in Figure 6d from the boxed region in 6c. Figure 6e augments the boxed region from the micrograph in 6c and positions it adjacent to the corresponding C EELS (overlaid with micrograph image in red) and overlaid EDX Al, C chemical maps for comparative purposes.

Figure 7 displays the initial performance of the catalyst as a function of methane, propane (C3), and butane (C4) products. A gradual drop in metal- and acid-site catalytic activity observed during initial testing. Red data points are associated with propane and butane generation resulting from early stage cracking by acidic sites on the γ-Al_2O_3 support.[13,14,27] Data points in black represent the production of methane resulting from early stage dehydrogenation reactions between the feed and the Pt−Re metal sites.[27] The steady decline in the production of both sets of data with TOS and the corresponding correlation with C growth and catalyst deactivation will be discussed in Section 4.3.

Along the lines of catalyst deactivation, chemical maps of C, Al were surveyed to assess the effects of coke growth in pore regions. Figure 8 gives one such example demonstrating the space filling nature of the coke. In panel 8a several regions with low levels of Al are marked by arrows. These same locations show rich C signals when the C, Al maps are overlaid with each other.

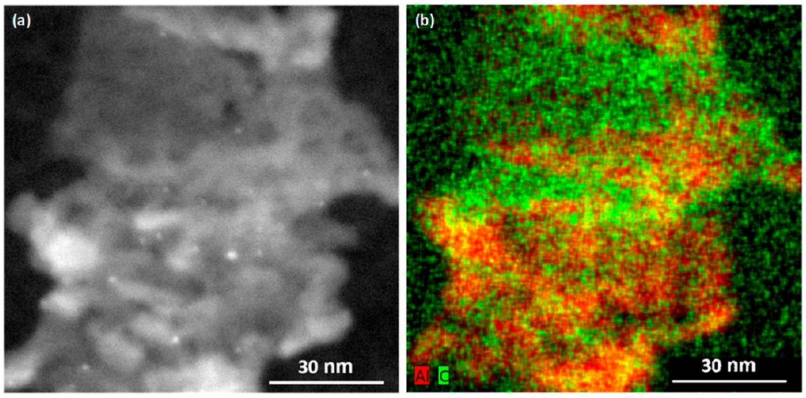

Figure 4. Chemical map shown adjacent to the (**a**) STEM micrograph for the region of interest in 10 h TOS sample. An overlaid chemical map is presented for (**b**) Al and C. Total scanning time was 20 m.

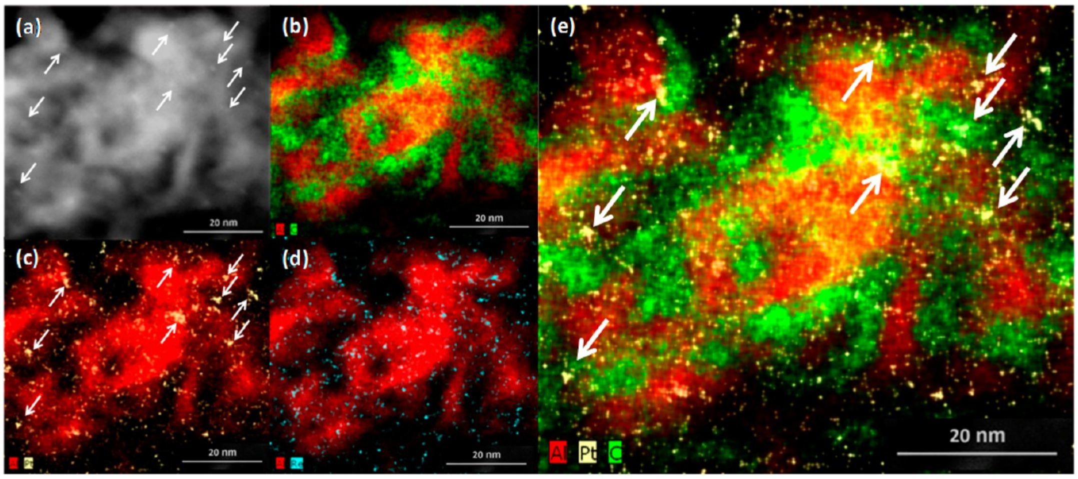

Figure 5. (**a**) STEM micrograph and corresponding chemical maps (**b**−**e**) for the region of interest are shown for the 96 h TOS sample. Chemical maps for (**b**) Al, C; (**c**) Al, Pt; and (**d**) Al, Re are presented. The map in (**e**) combines the chemical maps of Al, C, and Pt to show the spatial relationship between the coke and metal function. Arrows are included in (**a**), (**c**), and (**e**) to illustrate the coherence between X-ray signals and metal particle location in the original micrograph. Total scanning time was 13 m.

Chemical maps of a commercial catalyst (Figure 9) are shown after experiencing several months of process conditions. Next to the micrograph (9a) is the C, Al chemical map (9b) that shows the heterogeneity in the C signal in agreement with what was found for the 96 h sample. Chemical maps for the two metals (Pt and Re) used in the commercial catalyst, each overlaid with Al (Figure 9c and 9d for Pt and Re, respectively), show an unmistakable correlation between the Pt and Re chemical signals and the positions of the particles shown in the micrograph (Figure 9a). A combination of all four chemical maps (Al, C, Pt and Re) is shown in panel 9e to exhibit the relationship between the bimetallic nanoparticles and the coke.

4. DISCUSSION

4.1. Pt−Re Particle Characterization. The presence of several, individual, metal atoms unassociated with particles in a catalyst (Figure 1b) is a relatively new finding and garnered interest in the catalysis community.[28,29] Several studies have observed such features in working catalysts with some studies focusing on their catalytic activity.[30−32] In this case their presence indicates that complete interaction between all of the Pt and Re atoms does not occur despite the reduction process prior to testing. However, the observation that the amount of Re in the particles increases with increasing TOS (Figure 3 and Table 3) suggests that Pt−Re interactions scale with TOS. Table 3 shows that the fraction of Pt only particles decreases from fresh (46%) to 10 h TOS (42%) to 96 h TOS (33%). At the same time only subtle changes in particle size are observed (Figure 2a and Table 1), implying that the majority of individual metal atoms present on the support (Figure 1b) are likely Re and adjoin themselves to pre-existing Pt−Re particles during the reaction. This can be further supported by the steady decline in the approximate number of individual atoms per square area (Figure 2b, Table 2, and Table S1, Supporting Information) which is probably the source of the minute changes measured in particle size (Figure 2a) and in the increased levels of Re in the particles (Figure 3 and Table 3).

4.2. Coke Characterization. The ability to monitor chemical changes at such fine length scales even for low atomic number species (C, O, and N) is a testament to the recent improvements in analytical instrumentation[7] (although in the case of catalysts, collection time can be limited by beam sensitivity[8]). These enhancements have enabled characteristic differences between early and late coke formation. A clear difference between the two spent samples is the localization of the formed coke. After 10 h TOS (Figure 4) the chemical maps do not convey any distinguishing features of C other than that there is only a small amount on the catalyst surface. This can be

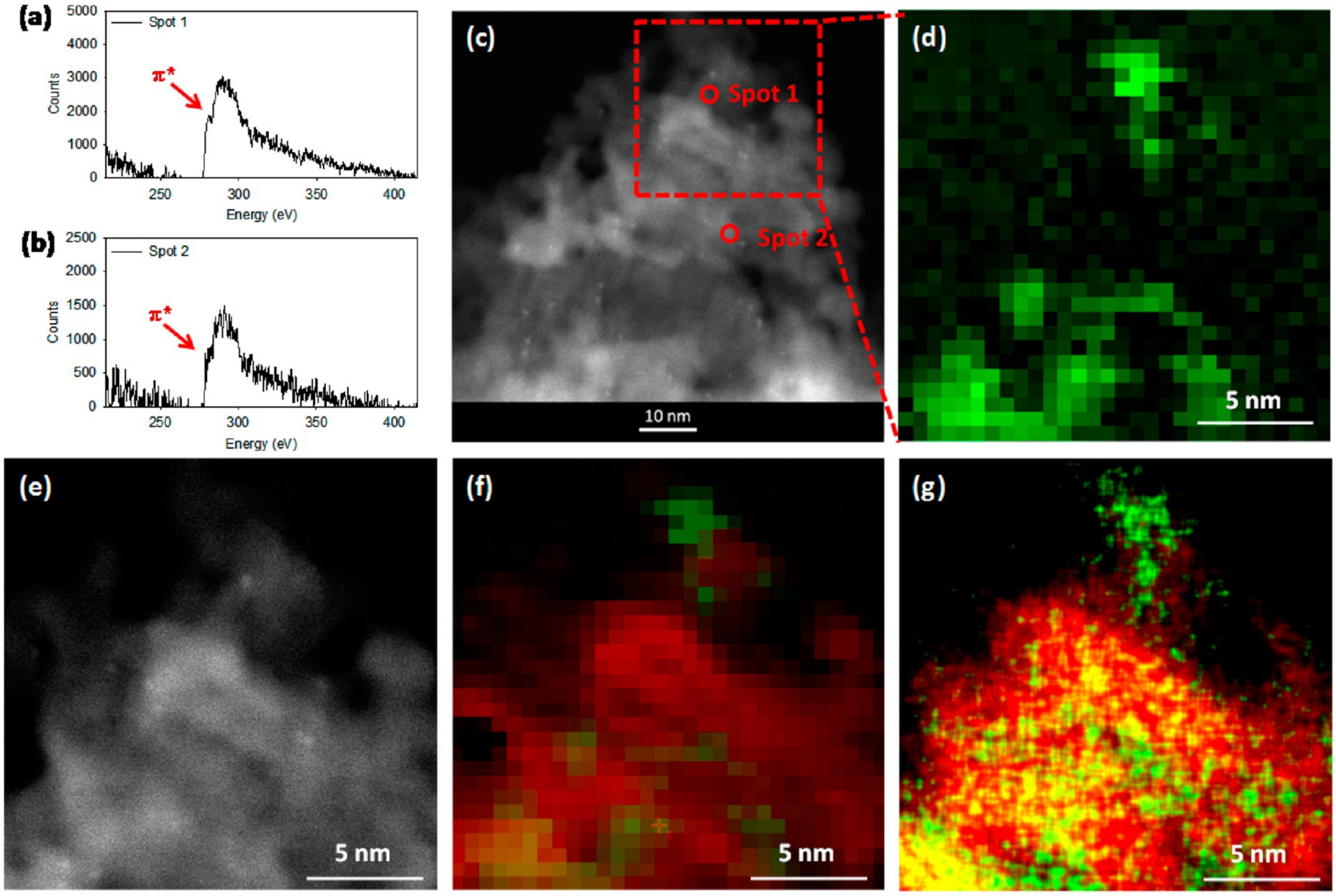

Figure 6. (a,b) EELS point spectra showing profile features associated with amorphous carbon for spots 1 and 2 annotated in (c) the micrograph. An areal EELS map (d) was collected scanning the outlined box (red dash) in (c), with (d) showing C signal heterogeneity. (e) The magnified micrograph for boxed region in (c) is placed in juxtaposition with (f) the C EELS map (green) overlaid with the image (red), and (g) EDX chemical map scanning the same region for C (green) and Al (red).

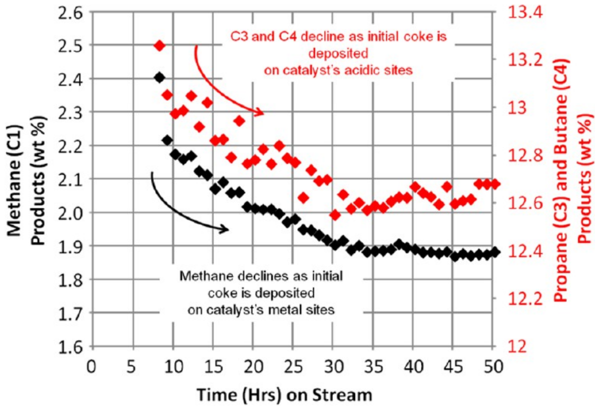

Figure 7. Initial drop in C1, C3, and C4 products monitored during catalyst testing.

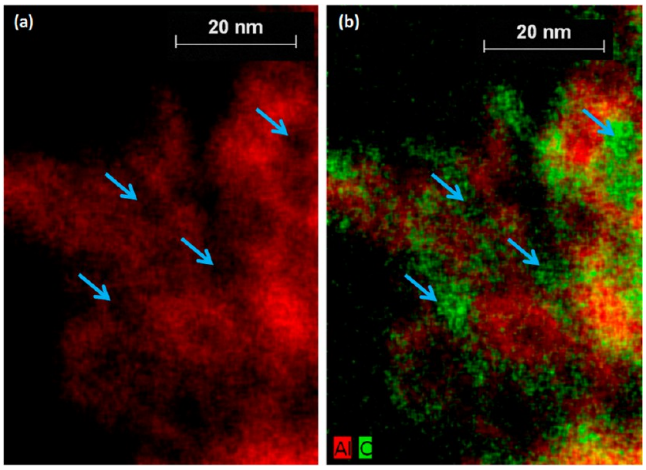

Figure 8. (a) Chemical map for Al with blue arrows pointing to Al-depleted regions likely pores. (b) Overlaying the Al map with the C map shows the coke to accrue in porous regions.

inferred from the background signals that almost match the intensity of C signals on the catalyst. Nevertheless Figure 4b promotes the idea of relatively uniform C/coke coverage.

Conversely, Figure 5b shows the C signal/coke represented heterogeneously on the catalyst. Distinct regions rich in coke are observed adjacent to regions with significantly lower levels of coke. From the chemical maps a pattern emerges after 96 h TOS where streams rich in C/coke appear to emanate from the metal sites (marked by arrows) leading to heterogeneity. This indicates that a transition has taken place where now coke growth is anisotropic when initially it was characterized as more homogeneous. Also significant are the chemical maps for Pt overlaid with Al (Figure 5c) that put on display localized signals for Pt in the bimetallic particles providing an unambiguous correlation between the map (5c) and the micrograph (5a). As

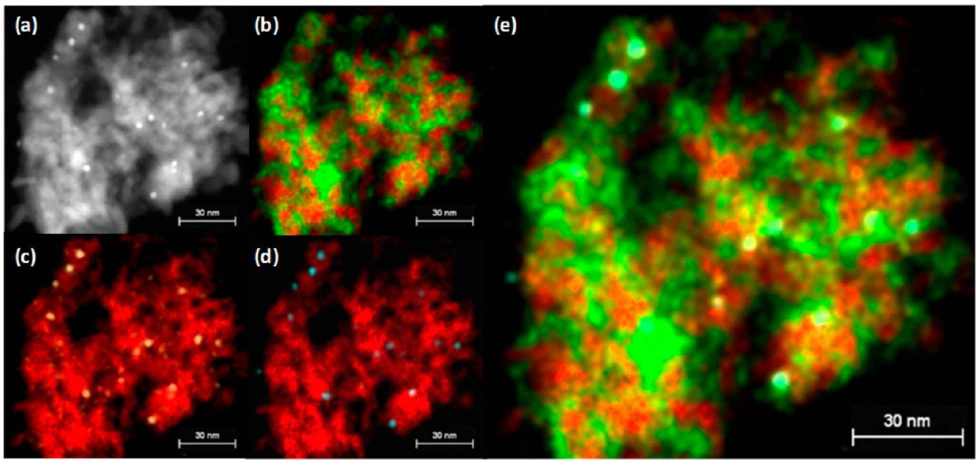

Figure 9. (**a**) STEM micrograph and corresponding chemical maps (**b**−**e**) for the region of interest in (**a**) are shown for the commercial catalyst. (**b**) Al, C; (**c**) Al, Pt; and (**d**) Al, Re; chemical maps are shown. The map in (**e**) combines all four elements (Al, C, Pt, and Re).

mentioned earlier, the lower Re loading (and lower interaction between Pt and Re, Figure 3 and Table 3) makes Re the sparser of the two metals resulting in a more diluted Re chemical map (Figure 5d). Figure 5c, on the other hand, shows clear evidence of the improved collection efficiency such that chemical mapping of subnanometer (0.78 nm, Table 1) supported particles is now possible with minimal damage to the sample (Figure S3 and S4, Supporting Information).

EELS is used to identify the allotrope of C represented on the sample after 96 h TOS. Point analyses at positions adjacent to the bimetallic particles showed the π^* pre-edge peak (and absence of σ^* peak) characteristic of amorphous carbon[6,33] (Figure 6a and b), in agreement with work done by others.[34] Comparison of the EELS (6f) and EDX (6g) chemical maps reinforces the EDX findings, which are as follows: (1) the coke is heterogeneous; (2) a correlation between the coke and the position of the Pt−Re metal sites exists. It is important to note that coke is present everywhere on the catalyst. Simply that the coke appears rich in specific regions does not indicate the absence of coke in regions where it appears depleted. It simply demonstrates considerable variability in C levels at the nanoscale on the γ-Al_2O_3 support for the 96 h TOS sample.

Given the breadth of Pt:Re stoichiometries (Figure 3) it became instructive to correlate coke dependence to particle composition. Figure S5 (Supporting Information) shows a trend following the regression line where increasing Re (mol %) in the particle appears to be associated with lower coke (wt %) for the sample after 10 h TOS. This is consistent with literature[19,35,36] reporting that the role of Re atom addition in reforming catalysts is to hydrogenate/crack adsorbed hydrocarbon into coke precursors (which are then desorbed to local support sites), minimizing coking severity and improving catalyst stability. A similar trend was observed for the 96 h sample (Figure S6, Supporting Information); however, the scatter associated with the data make any correlation unconvincing. We attribute the scatter to excessive amounts of coke saturating the catalyst. Combustion analysis confirms the significant differences in coke levels between the two samples: 0.6 wt % C (10 h) and 11 wt % C (96 h).

This brings us to a separate mode of coke-induced catalyst deactivation made observable by chemical imaging that must be taken into consideration. Coke is not limited to direct blockage of active sites as the only approach to lowering catalyst performance. Figure 8 presents one of many examples where porous regions on the γ-Al_2O_3 appear to have high amounts of C. This is an important observation because the accumulation of C at pore sites impedes passage of unreacted feed to active sites within the γ-Al_2O_3 matrix. Indirectly, it disables effective diffusion of hydrocarbon feed in and out of the catalyst. As a result, the activity of the material is limited by the restricted access to active components in the catalyst and leads to a drop in performance. Other studies have indirectly suggested and demonstrated the effects of pore-blockage,[37,38] here we show empirical data visually revealing pore-blockage using chemically distinct X-ray signals at nanometer length scales.

4.3. Coking Mechanism.

Empirical differences in coke formation between Figures 3b and 4b need to be addressed to understand the divergence in such characteristic features (homogeneous vs heterogeneous coke formation). Based on the chemical map after 96 h TOS we are presented with a form of coking that appears to be associated with the position of the metal sites. Coke grows directionally up to a distance of 20−30 nm away from the metal sites, consistent with reports by others.[34,39] These features have been noted before and align with results found by Gallezot et al. using transmission electron microscopy (TEM) and EELS.[34] In the aforementioned study the coking mechanism was ascribed to dehydrogenation of hydrocarbon in the feed by metal nanoparticles which would “spill over” onto the support. Via cyclic condensation, highly acidic sites on the γ-Al_2O_3 convert the unsaturated hydrocarbon to aromatic species which polymerize eventually leading to refractory coke/amorphous C. This mechanism is in-line with our chemical mapping data where coke appears to originate from metal sites but disseminates linearly. However, it neglects the initial coking stage that occurs where C signals are more uniformly dispersed as was seen for the sample after 10 h TOS. It has been shown by TPO[25] and infrared (IR) analysis of adsorbed CO[12] that coke exists both on the metal sites and support sites of a functioning Pt−Re catalyst. A mechanism of coke formation was suggested by Myer[40] in a study of Pt on SiO_2 and η-Al_2O_3. Their study was able to draw a parallel between octane loss and catalyst deactivation, where coke (or coke precursors) deposits on the metal and subsequently transfer to the support to react further.

We propose that coke formation occurs in a two stage process. In the first stage, coke precursors homogeneously deposit on the catalyst surface on both metallic and acidic sites. This is confirmed by Figure 7 where an overall drop in the activity indicates the rapid, initial attenuation of all active sites (metal and acidic) indiscriminately. In the second stage a steady coking mechanism, as described above, occurs where coke precursors formed by dehydrogenation "spill over" onto acidic support sites leading to streams of coke flowing from the bimetallic particles, as evidenced by the observed heterogeneity in the EDX (and EELS) chemical maps. This is further supported by Figure 7 where the attenuation of the active sites levels off; whereas coke levels continue to rise indicating coke is accumulating on the catalyst affecting it in a different way. In the current study stabilization occurs at about 30 h TOS at which point we believe the steady growth of coke streams occurs.

Comparisons between the pilot plant tested samples and actual commercial samples were made to prove the heterogeneity observed is not isolated to pilot plant experiments but is universally applicable to commercial reforming processes. The commercial samples analyzed were severely coked (~ 20 wt % C) having experienced several months of operation (significantly different from 10 or 96 h TOS). To summarize the findings, the same mechanistic trends with respect to coking were observed. Initially, coke was found to be homogeneously distributed throughout the catalyst material (Figure S7, Supporting Information, spent catalyst 10 h TOS ~ 1 wt % C). After several months of operation, a clear heterogeneity emerged that was closely associated with the spatial distribution of the metal particle sites which have increased in size as result of process conditions. Chemical maps for the latter sample are shown in Figure 9. A micrograph of the scanned region is displayed in Figure 9a in juxtaposition with the C and Al chemical map in panel 9b demonstrates the same heterogeneous nature of the coke on γ-Al_2O_3 found for the 96 h TOS sample. Figures 9c and 9d show the chemical maps of Pt and Re, respectively overlaid with Al leaving little doubt as to the efficiency of X-ray detection as they are directly coherent with the corresponding micrograph image (9a); the spatial distribution of the metal sites identified by the *Z*-contrast imaging[4] match perfectly with those identified by EDX detection. This can be attributed to the advanced detection system but also to the increase in mean particle size with TOS which on average doubled (1.2 nm, Figure S8, Supporting Information). It is possible that particle growth was achieved by individual atom migration to particles or by particle−particle coarsening. Catalytically, this has implications since an increase in particle size limits the dispersion of the metal active sites resulting in a less active material. Lastly, a compilation of the four elemental maps (9e) demonstrates the association of coke streams with the bimetallic particles on the γ-Al_2O_3 support. As was observed with the pilot plant sample (Figure 5e), the streams of coke in Figure 9e are seen to originate from the metal sites. It is interesting to note that even at 20 wt % C after months on stream (compared to 11 wt % C for the 96 h TOS) the commercial samples continue to show the same heterogeneous pattern of coke growth on the catalyst further verifying the coking mechanism described herein.

5. CONCLUSIONS

Chemical maps were used to establish a spatial relationship between carbonaceous deposits/coke and the metal sites on a reforming catalyst. The coke formed from precursors initially deposits on the catalyst and is shown to be homogeneously distributed, attenuating all active sites. Characterization of the Pt−Re nanoparticles revealed anisotropic coke growth stemming from the metal sites (and quantifiable changes to the composition of the metal function with TOS). These data support the theory that coke precursors are displaced from the metal sites onto the support where acidic sites induce polymerization. As revealed by EELS analyses, the end products appear to be streams of amorphous C flowing from the Pt−Re nanoparticles. Comparison with a catalyst from a commercial demonstrated exhibited identical behavior to what was found during pilot plant testing. Other types of catalytic systems with different formulations may exhibit different coking and morphologies. With the acquisition of C_s-STEM and advanced X-ray sensing technology, there now exists a method by which the nature of coke formation can be characterized. From the perspective of catalyst preparation the prospects are very attractive as findings, such as those presented here, can be employed to optimize the formulation of catalytic materials such that they exhibit greater tolerance toward coke deactivation.

ASSOCIATED CONTENT

Ⓢ Supporting Information

Supplementary chemical maps, micrographs showing minor effects of beam damage, and plots showing the dependence of localized coke on particle composition, tables for statistical data, and size distribution histogram for the commercial sample. This material is available free of charge via the Internet at http://pubs.acs.org.

AUTHOR INFORMATION

Corresponding Author

*E-mail: Sergio.Sanchez5@Honeywell.com.

Notes

The authors declare no competing financial interest.

REFERENCES

(1) Herzing, A. A.; Kiely, C. J.; Carley, A. F.; Landon, P.; Hutchings, G. J. *Science* **2008**, *321*, 1331−1335.

(2) Gontard, L. C.; Chang, L.-Y.; Hetherington, C. J. D.; Kirkland, A. I.; Ozkaya, D.; Dunin-Borkowski, R. E. *Angew. Chem.,. Int. Ed.* **2007**, *46*, 3683−3685.

(3) Li, Z. Y.; Young, N. P.; Di Vece, M.; Palomba, S.; Palmer, R. E.; Bleloch, A. L.; Curley, B. C.; Johnston, R. L.; Jiang, J.; Yuan, J. *Nature* **2008**, *451*, 46−48.

(4) Varela, M.; Lupini, A. R.; Van Benthem, K.; Borisevich, A. Y.; Chisholm, M. F.; Shibata, N.; Abe, E.; Pennycook, S. J. *Annul. Rev. Mater. Res.* **2005**, *35*, 539−569.

(5) Xin, H. L.; Mundy, J. A.; Liu, Z.; Cabezas, R.; Hovden, R.; Kourkoutis, L. F.; Zhang, J.; Subramanian, N. P.; Makharia, R.; Wagner, F. T.; Muller, D. A. *Nano Lett.* **2012**, *12*, 490−497.

(6) Ahn, C. C. *Transmission Electron Energy Loss Spectrometry in Material Science and the EELS Atlas*; Wiley: Weinheim, Germany, 2004.

(7) Schlossmacher, P.; Klenov, D. O.; Freitag, B.; von Harrach, S.; Steinbach, A. *Microsc. Anal.* **2010**, *24*, S5−S8.

(8) Lakis, R. E.; Lyman, C. E.; Stenger, H. G. *Symposium on Catalyst Support: Chemistry, Forming and Characterization* **1991**, *36*, 523.

(9) Loos, J. *Adv. Mater.* **2005**, *17*, 1821−1833.

(10) Satoh, N.; Nakashima, T.; Kamikura, K.; Yamamoto, K. *Nat. Nanotechnol.* **2008**, *3*, 106−111.

(11) Buining, P. A.; Humbel, B. M.; Philipse, A. P.; Verkleij, A. J. *Langmuir* **1997**, *13*, 3921−3926.

(12) Sanchez, S. I.; Bradley, S. A.; Sinkler, W. *Microsc. Microanal.* **2012**, *18* (S2), 1036−1037.

(13) Meyers, R. A. *Handbook of Petroleum Refining Processes*, 3rd ed.; McGraw Hill: New York, 2004.

(14) Antos, G. J.; Aitani, A. M.; Parera, J. M. *Catalytic Naphtha Reforming*, 2nd ed.; Marcel Dekker, Inc.: New York, 2004.

(15) Little, D. M. *Catalytic Reforming*; PennWell Publishing Co.: Tulsa, OK, 1985.

(16) Santos, M. C. S.; Grau, J. M.; Pieck, C. L.; Parera, J. M.; Fierro, J. L. G.; Figoli, N. S.; Rangel, M. C. *Catal. Lett.* **2005**, *103*, 229−237.

(17) Xiao, J.; Puddephatt, R. J. *Coord. Chem. Rev.* **2005**, *143*, 457−500.

(18) Mazzieri, V. A.; Grau, J. M.; Yori, J. C.; Vera, C. R.; Pieck, C. L. *Appl. Catal., A* **2009**, *354*, 161−168.

(19) Augustine, S. M.; Alameddin, G. N.; Sachtler, W. M. H. *J. Catal.* **1989**, *115*, 217−232.

(20) Rønning, M.; Gjervan, T.; Prestvik, R.; Nicholson, D. G.; Holmen, A. *J. Catal.* **2001**, *204*, 292−304.

(21) Isaacs, B. H.; Petersen, E. E. *J. Catal.* **1982**, *77*, 43−52.

(22) Bertolacini, R. J.; Pellet, R. J. In *Catalyst Deactivation: Proceedings of the International Symposium*, Antwerp, The Netherlands, Oct 13−15, 1980; Delmon, B., Froment, G. F., Eds.; Elsevier: Amsterdam, The Netherlands, 1980; Vol. *6*.

(23) Ribeiro, F. H.; Bonivardi, A. L.; Kim, C.; Somorjai, G. A. *J. Catal.* **1994**, *150*, 186−198.

(24) Jovanović, M. R.; Putanov, P. S. *Appl. Catal., A* **1997**, *159*, 1−7.

(25) Pieck, C. L.; Marecot, P.; Barbier, J. *Appl. Catal., A* **1996**, *145*, 323−324.

(26) Anderson, J. A.; Chong, F. K.; Rochester, C. H. *J. Mol. Catal. A* **1999**, *140*, 65−80.

(27) Boyle, J. P. European Patent No. EP0463851B1, 1991; ESSO Engineering (Europe) Ltd. Patents & Licences: Leatherhead, Surrey.

(28) Boyes, E. D.; Ward, M. R.; Lari, L.; Gai, P. L. *Ann. Phys.* **2013**, *6*, 423−429.

(29) Bradley, S. A.; Sinkler, W.; Blom, D. A.; Bigelow, W.; Voyles, P. M.; Allard, L. F. *Catal. Lett.* **2012**, *142*, 176−182.

(30) Qiao, B.; Wang, A.; Yang, X.; Allard, L. F.; Jiang, Z.; Cui, Y.; Liu, J.; Li, J.; Zhang, T. *Nat. Chem.* **2011**, *3*, 634−641.

(31) Zhang, X.; Guo, J.; Guan, P.; Liu, C.; Huang, H.; Xue, F.; Dong, X.; Pennycook, S. J.; Chisholm, M. F. *Nat. Commun.* **2011**, *4*, 1924.

(32) Bayram, E.; Lu, J.; Aydin, C.; Uzun, A.; Browning, N. D.; Gates, B. C.; Finke, R. G. *ACS Catal.* **2012**, *2*, 1947−1957.

(33) Sanchez-Lopez, J. C.; Erdemir, A.; Donnet, C.; Rojas, T. C. *Surf. Coat. Technol.* **2003**, *163−164*, 444−450.

(34) Gallezot, P.; Leclercq, C.; Barbier, J.; Marecot, P. *J. Catal.* **1989**, *116*, 164−170.

(35) Shum, V. K.; Butt, J. B.; Sachtler, W. M. H. *J. Catal.* **1986**, *99*, 126−139.

(36) Augustine, S. M.; Sachtler, W. M. H. *J. Catal.* **1987**, *106*, 417−427.

(37) Van Donk, S.; Bitter, J. H.; de Jong, K. P. *Appl. Catal., A* **2001**, *212*, 97−116.

(38) Menon, P. G. *J. Mol. Catal.* **1990**, *59*, 207−220.

(39) Chang, T. S.; Rodriguez, N. M.; Baker, R. T. K. *J. Catal.* **1990**, *123*, 486−495.

(40) Myers, C. G.; Lang, W. H.; Weisz, P. B. *Ind. Eng. Chem.* **1961**, *53*, 299−302.